Science of the Total Environment 912 (2024) 169411

Contents lists available at ScienceDirect

Science of the Total Environment

journal homepage: www.elsevier.com/locate/scitotenv

Regional background ozone estimation for China through data fusion of observation and simulation

Zhixu Sun [a,b], Jiani Tan [a,b], Fangting Wang [a,b], Rui Li [a,b], Xinxin Zhang [a,b], Jiaqiang Liao [a,b], Yangjun Wang [a,b], Ling Huang [a,b], Kun Zhang [a,b], Joshua S. Fu [c], Li Li [a,b,*]

[a] School of Environmental and Chemical Engineering, Shanghai University, Shanghai 200444, China
[b] Key Laboratory of Organic Compound Pollution Control Engineering (MOE), Shanghai University, Shanghai 200444, China
[c] Deparent of Civil and Environmental Engineering, University of Tennessee, Knoxville, TN 37996, USA

HIGHLIGHTS

- The regional background O_3 concentration in China is estimated at 35 ± 4 ppb in 2020.
- O_{3_RBG} accounts for 81 % and 55 % of MDA8 O_3 in clean and polluted conditions, respectively.
- O_{3_RBG} dominates MDA8 O_3 (>85 %) for all Chinese regions when O_3 is lower than 60 ppb.
- Natural emissions contribute more significantly to O_{3_RBG} in China compared to meteorological factors.

GRAPHICAL ABSTRACT

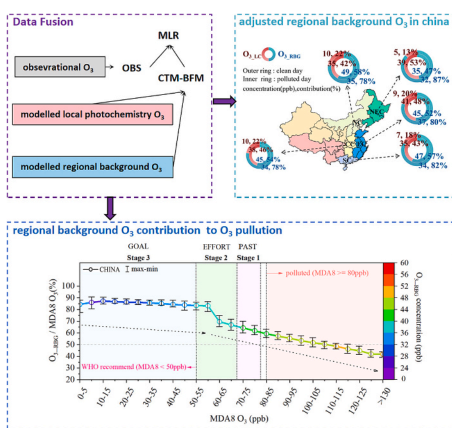

ARTICLE INFO

Editor: Philip K. Hopke

Keywords:
Regional background O_3
Multiple linear regression
Chemical transport model
Brute force method
China

ABSTRACT

Regional background ozone (O_{3_RBG}) is an important component of surface ozone (O_3). However, due to the uncertainties in commonly used Chemical Transport Models (CTMs) and statistical models, accurately assessing O_{3_RBG} in China is challenging. In this study, we calculated the O_{3_RBG} concentrations with the CTM – Brute Force Method (BFM) and constrained the results with site observations of O_3 with the multiple linear regression (MLR) model. The annual average O_{3_RBG} concentration in China region in 2020 is 35 ± 4 ppb, accounting for 81 ± 5 % of the maximum 8-h average O_3 (MDA8 O_3). We applied the random forest and Shapley additive explanations based on meteorological standardization techniques to separate the contributions of meteorology and natural emissions to O_{3_RBG}. Natural emissions contribute more significantly to O_{3_RBG} than meteorology in various Chineses regions (30–40 ppb), with higher contributions during the warm season. Meteorological factors show higher contributions in the spring and summer seasons (2–3 ppb) than the other seasons. Temperature and humidity are the primary contributors to O_{3_RBG} in regions with severe O_3 pollution in China, with their individual impacts ranging from 30 % to 62 % of the total impacts of all meteorological factors in different seasons.

* Corresponding author at: School of Environmental and Chemical Engineering, Shanghai University, Shanghai 200444, China.
E-mail address: Lily@shu.edu.cn (L. Li).

https://doi.org/10.1016/j.scitotenv.2023.169411
Received 24 September 2023; Received in revised form 5 December 2023; Accepted 13 December 2023
Available online 19 December 2023

For policy implications, we tracked the contributions of O_{3_RBG} and local photochemical reaction contributions (O_{3_LC}) to total O_3 concentration at different O_3 levels. We found that O_{3_LC} contribute over 45 % to MDA8 O_3 on polluted days, supporting the current Chinese policy of reducing O_3 peak concentrations by cutting down precursor emissions. However, as the contribution of O_{3_RBG} is not considered in the policy, additional efforts are needed to achieve the control groal of O_3 concentration. As the implementation of stringent O_3 control measurements in China, the contribution of O_{3_RBG} become increasingly significant, suggesting the need for attention to O_{3_RBG} and regional joint prevention and control.

1. Introduction

Ozone (O_3) is a secondary air pollutant formed by the photochemical reactions of nitrogen oxides (NOx) and volatile organic compounds (VOCs) under the presence of sunlight (Zheng et al., 2023). Elevated surface O_3 level is detrimental to human health due to its potent oxidizing properties (Gu et al., 2022; Hong and Chen, 2020; Lelieveld et al., 2015; World Health Organization. Regional Office for, E, 2021). It also poses risks to animals, plants, and their habitats, leading to a decline in global food production and disrupting the balance of the ecosystems (Yue et al., 2017). Additionally, O_3 plays an important role in the global atmospheric radiation balance (Barnes et al., 2023; Rasmussen et al., 2013) and can consequently influence atmospheric circulations (Rudeva et al., 2023). The annual O_3 concentrations in China have been consistently increasing by about 5 % per year during 2016–2020 (Guo et al., 2023; Huang et al., 2018; Lu et al., 2020; Silver et al., 2018; Zheng et al., 2017). The concentrations decreased by 1–2 μg/m^3 in 2020 and 2021 but rebounded by 5.8 % in 2022, leading to the exceedance of China's air quality standard of MDA8 O_3 (80ppb) in 91 cities (https://www.mee.gov.cn/). O_3 pollution has been a critical challenge facing China and has become the focus of the scientific communities and government agencies.

The surface O_3 concentration is the sum of regional background O_3 (O_{3_RBG}) and O_3 formed via local photochemical reactions (O_{3_LC}). O_{3_RBG} is defined as the O_3 concentrations in the absence of anthropogenic sources (Lu et al., 2019). It is mainly generated from natural sources such as biogenic volatile organic compounds (BVOCs), soil nitrogen oxides (SNOx), lightning NOx (LNOx), wildfires, and methane oxidation (Li et al., 2022; McDonald-Buller et al., 2011), and from stratosphere-troposphere exchange (Knowland et al., 2017) and long-range transport (Mathur et al., 2022). On one hand, the implementation of anthropogenic emission control and management policies by government agencies is promising for the reduction of O_{3_LC} (Li et al., 2021). On the other hand, O_{3_RBG} has contributed to the increase of O_3 concentrations in the past decade, mainly due to the promoted natural emissions due to changes in meteorological conditions (Chen et al., 2022; Lu et al., 2019). Therefore, investigation of the characteristics of O_{3_RBG} is of great importance in the mitigation of O_3 pollution.

It has been reported that O_{3_RBG} accounts for about 70–80 % of the surface O_3 concentrations in China (Chen et al., 2022; Lu et al., 2019), but there leave large uncertainties. Three methods have been commonly used to estimate the O_{3_RBG} concentrations: (1) Estimation by observed

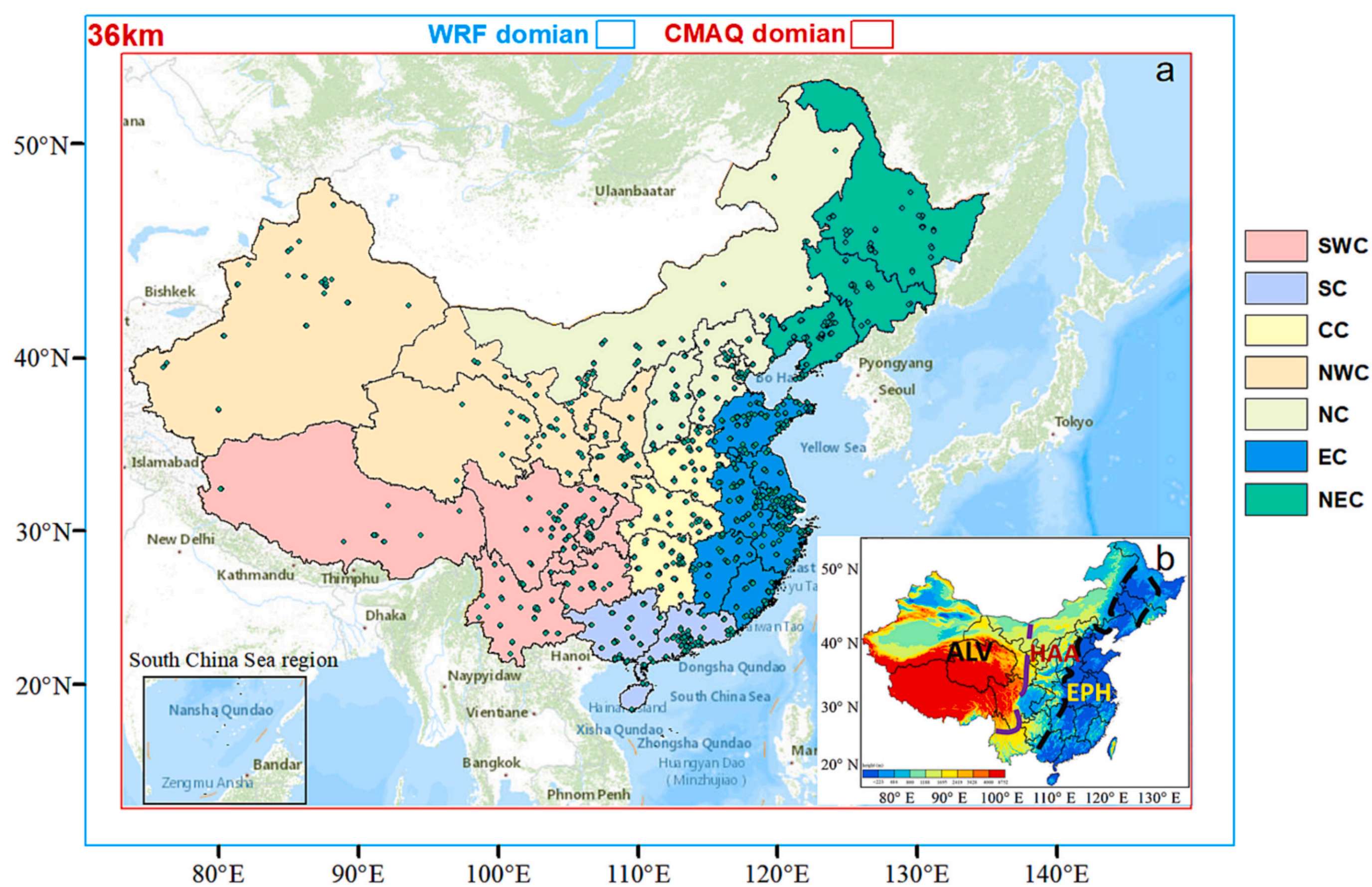

Fig. 1. Study domain. (a) Green dots represent the locations of the national air quality monitoring stations. Background colors represent the divisions of seven geographic regions. (b) China's topographic map and the three regions classified by climate, altitude, and emission sources.

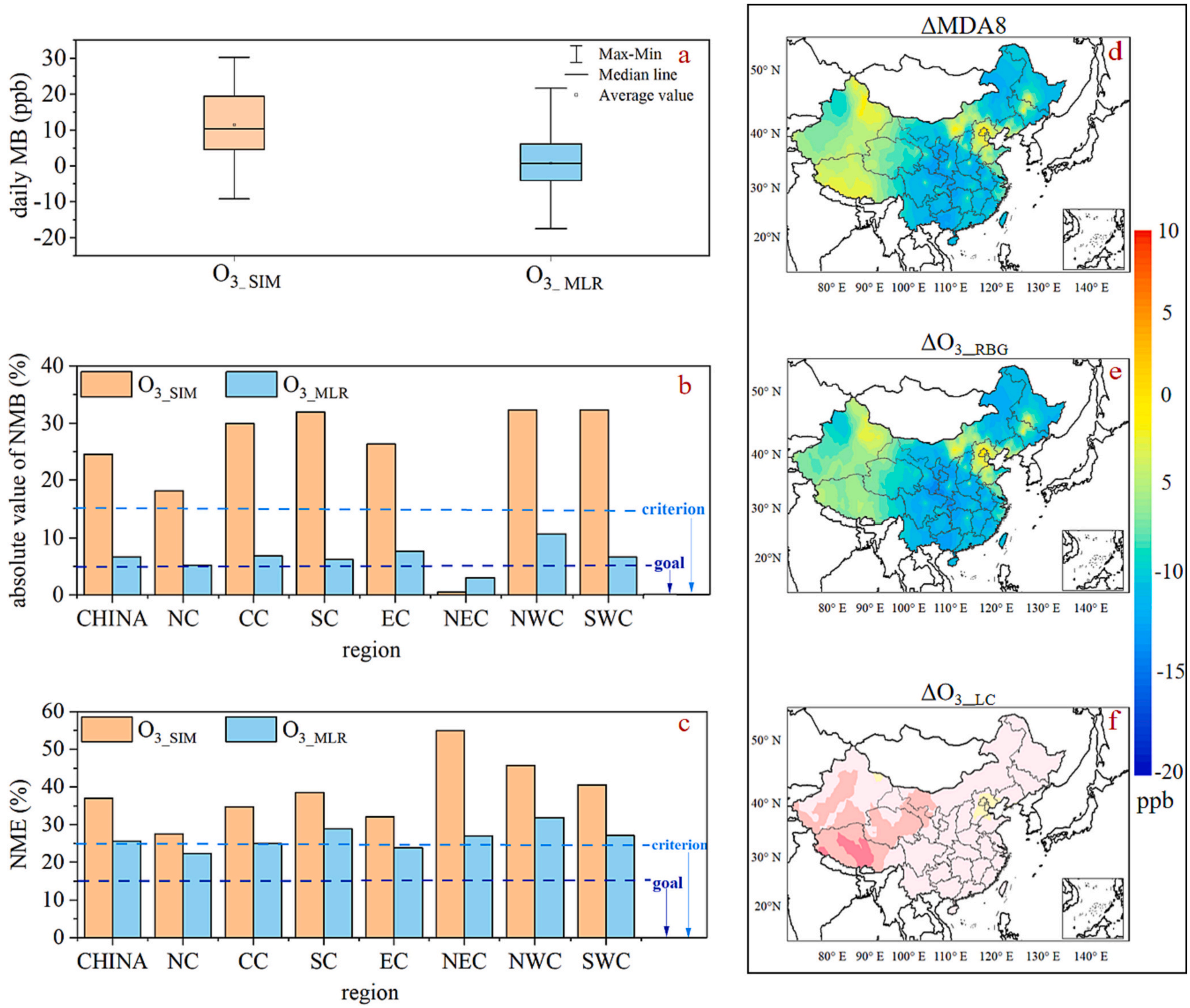

Fig. 2. (a) Boxplot of the performances of the WRF-CMAQ (O_{3_SIM}) and MLR model (O_{3_MLR}) on simulating O_3 concentrations presented by mean bias (MB) of O_{3_SIM} (in orange) and the MB of O_{3_MLR} (in blue). The center line of the box represents the median, the square represents the mean, and the upper and lower edges of the box represent the 25th and 75th percentiles, respectively. (b, c) Performances of O_{3_SIM} and O_{3_MLR} for China and seven regions presented by normalized mean bias (NMB) and normalized mean error (NME). (d-f) Differences between MLR-adjusted and WRF-CMAQ simulated annual average concentrations of MDA8 O_3 (d), O_{3_RBG} (e) and O_{3_LC} (f). The values are calculated as (MLR – WRF-CMAQ).

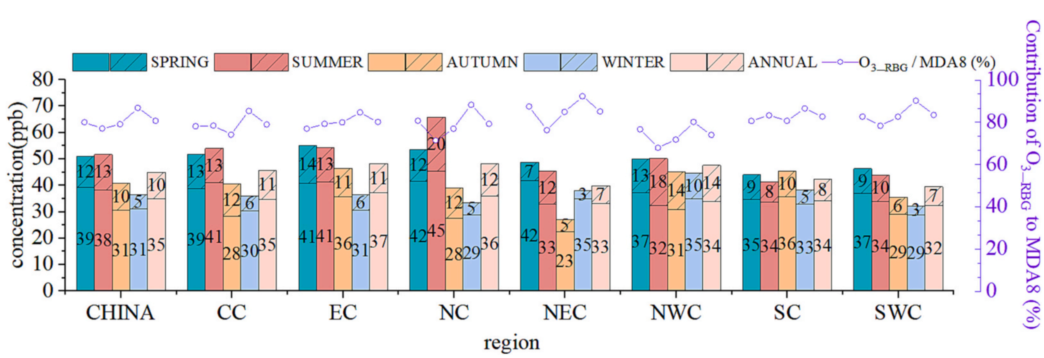

Fig. 3. O_{3_RBG} and O_{3_LC} in China and specific regions in 2020. The column chart shows O_{3_RBG} without a line and O_{3_LC} with a line. The horizontal axis indicates different regions in China. The left vertical axis represents O_3 concentrations levels, with green, red, orange, blue, and pink colors representing spring, summer, autumn, winter, and annual averages, respectively. The purple dots line and the right vertical axis represents the proportion of O_{3_RBG} to MDA8 O_3.

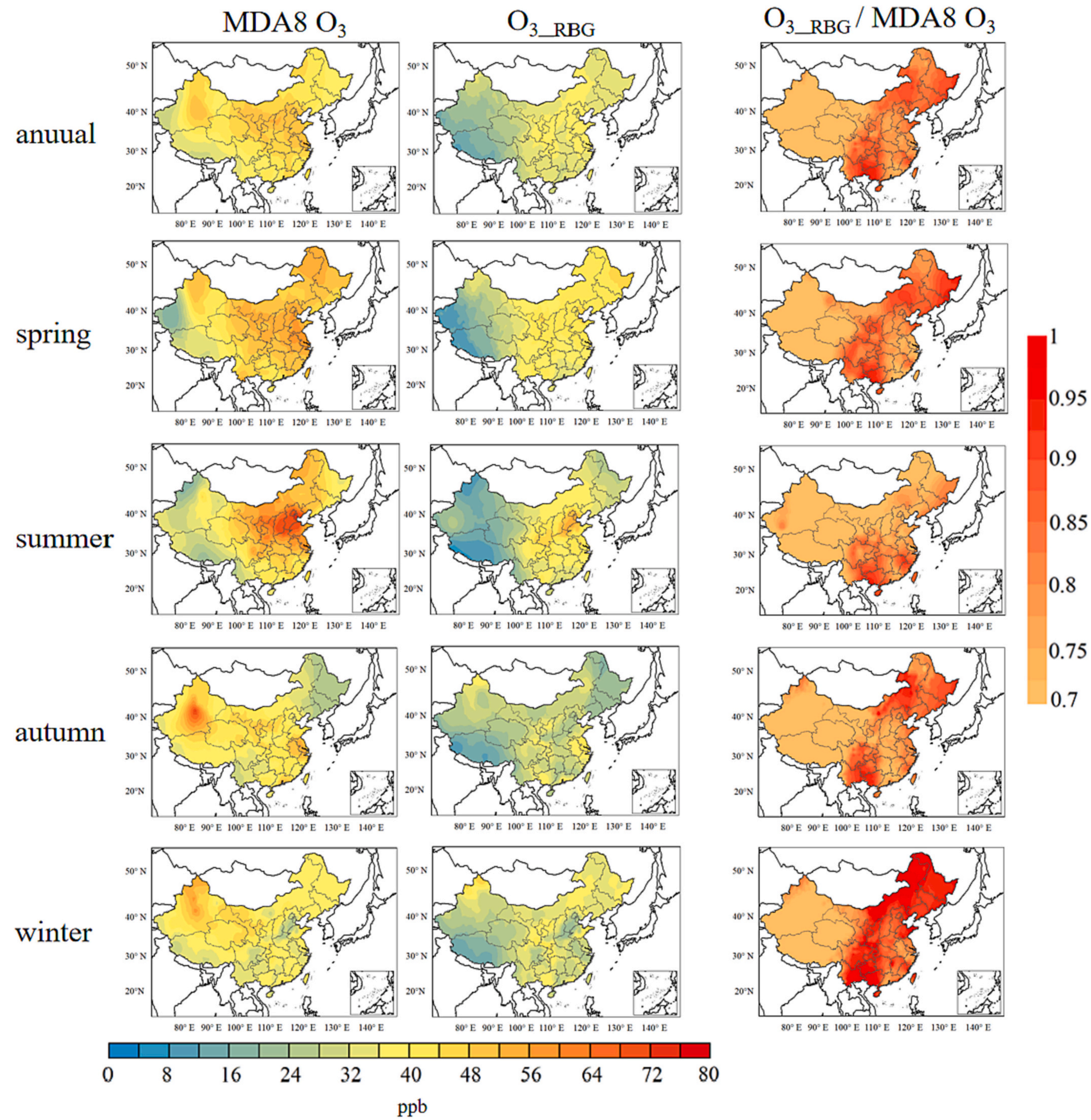

Fig. 4. Spatial distribution of O_{3_RBG} and the proportion of O_{3_RBG} in MDA8 O_3. Seasons are represented on the horizontal axis, and O_3 categories (MDA8 O_3, O_{3_RBG}, the proportion of O_{3_RBG} in MDA8 O_3) on the vertical axis.

O_3 at remote monitoring sites. However, it is difficult to avoid the influence of extensive human activities (Vingarzan, 2004). (2) Application of statistical methods such as principal component analysis (PCA) (Suciu et al., 2017), and Hidden Markov Models method (HMM) (Rizos et al., 2022). The PCA method determines the principal concentrations of O_3 at an observational site using an orthogonal matrix approach and considers it as the O_3 background concentrations. The HMM method categorizes the O_3 concentrations in a time-series dataset based on features such as anomalies and daily amplitude. This allows for the categorization of O_3 concentrations under different scenarios. The O_3 concentrations of the most stable and predominant scenario are considered as the background O_3. However, the statistical methods are based on mathematical relationships without references to the chemical and physical mechanisms regarding O_3 formation. (3) Application of the chemical transport models (CTM) (Atherton et al., 1996). This approach takes advantage of emulating the atmospheric reactions driven by chemical and physical processes and can therefore address the shortcomings of the statistical models. The CTM approach distinguishes the O_{3_RBG} from the total O_3 by the Brute Force Method (BFM) (Cheng et al., 2017; Skipper et al., 2021). The BFM approach reduces the emissions of the precursors (for example, anthropogenic NO*x* emissions) and simulates the changes in the concentrations of air pollutants (for example, O_3 concentration) (Zhang

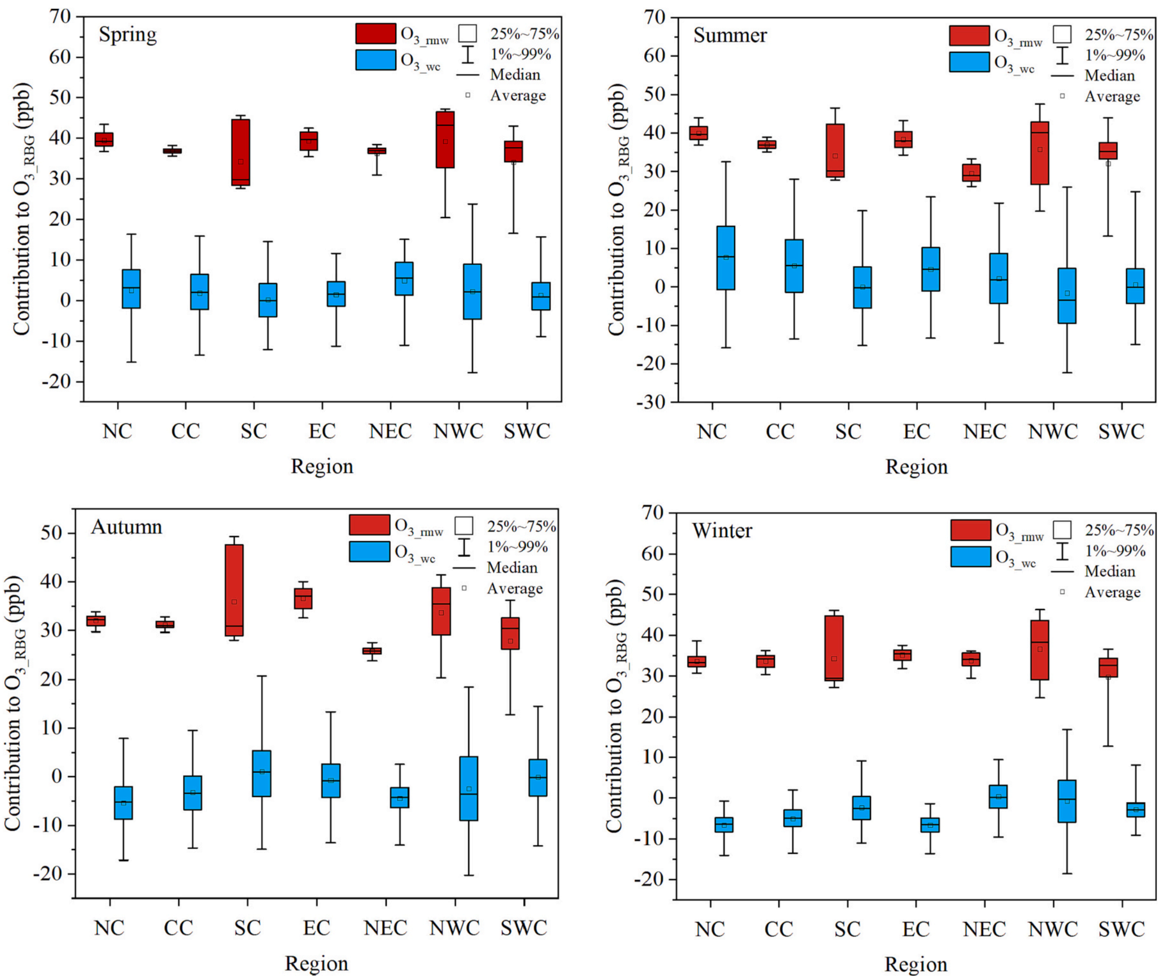

Fig. 5. The hourly concentrations of O_{3_rmw} and O_{3_wc} in different seasons. (a) to (d) correspond to the spring, summer, autumn, and winter seasons, respectively. The blue boxplots represent O_{3_wc}, while the red boxplots represent O_{3_rmw}. The vertical axis represents concentration, and the horizontal axis represents regions.

et al., 2014). However, the BFM approach could overlook the nonlinearity between the emission reduction and response to air pollution (Xie et al., 2022; Zheng et al., 2018). Additionally, the CTM results are deviated from site observations of O_3 due to the uncertainties in model inputs (for example, emission inventories and meteorological fields), and parameterization (for example, radiation scheme and gas chemistry mechanism) (Huang et al., 2019; Wang et al., 2022b; Xu et al., 2021).

The obstacles above-mentioned quantification methods led to a vague understanding of O_{3_RBG}, which is indicated by the inconsistent estimations from different studies. For example, Wang et al. (2011) used the Goddard Earth Observing System with Chemistry (GEOS-CHEM) model and reported that the annual O_{3_RBG} concentrations ranged between 25–55 ppb in different regions of China. Li et al. (2012) used the Community Multiscale Air Quality Modeling System - Ozone Source Apportionment Technology (CAMx-OSAT) to analyze O_{3_RBG} in the Pearl River Delta region of China and obtained 5–10 ppb higher results than that of Wang et al. (2011). Li et al. (2018) ran the WRF-CHEM model and found that O_{3_RBG} contributed 10–25 ppb in northwestern China, which is 30 % lower than the assessments reported by Wang et al. (2011). Chen et al. (2022) quantified the O_{3_RBG} via the relationship between temperature and O_3, and found that the O_{3_RBG} values during the warm season in China ranges from 50 to 55 ppb, which are 10 ppb higher than the values estimated by the GEOS-CHEM results by Lu et al. (2019) and Wang et al. (2011).

This study aims to improve our understanding of the O_{3_RBG} concentrations and their role in the mitigation of O_3 pollution in China. We simulated the O_{3_RBG} and O_{3_LC} by the CTM-BFM approach for China for the year 2020. The results are then constrained by the observed O_3 concentrations from monitoring sites with the multiple linear regression (MLR) model to derive the adjusted O_{3_RBG} and O_{3_LC}. On these bases, we investigated the spatial and seasonal variations of O_{3_RBG} concentrations and discussed the major driving factors. Finally, we discussed the contribution of O_{3_RBG} to total O_3 pollution and gave insights into the mitigation of O_3 pollution in China.

2. Methodology

2.1. Site observations

Site observations of O_3 (O_{3_OBS}) were collected from the National Air Quality Monitoring Stations (AQMS) for the year 2020 (https://quotsoft.net/air/). We collected hourly data from 1462 sites (Fig. 1). The MDA8 O_3 concentrations (523,953 data sets in total) were used to evaluate the WRF-CMAQ model performance and build the MLR model. We also obtained the longitude, latitude, and altitude information of the stations for the MLR model. The meteorological data including temperature, relative humidity, wind speed, and wind direction with hourly temporal resolution were collected from the monitoring stations of the National Meteorological Bureau to evaluate the WRF performance (http://data.cma.cn/data). All data were preprocessed to exclude zero and negative values and outliners (see details in Xue et al., 2023).

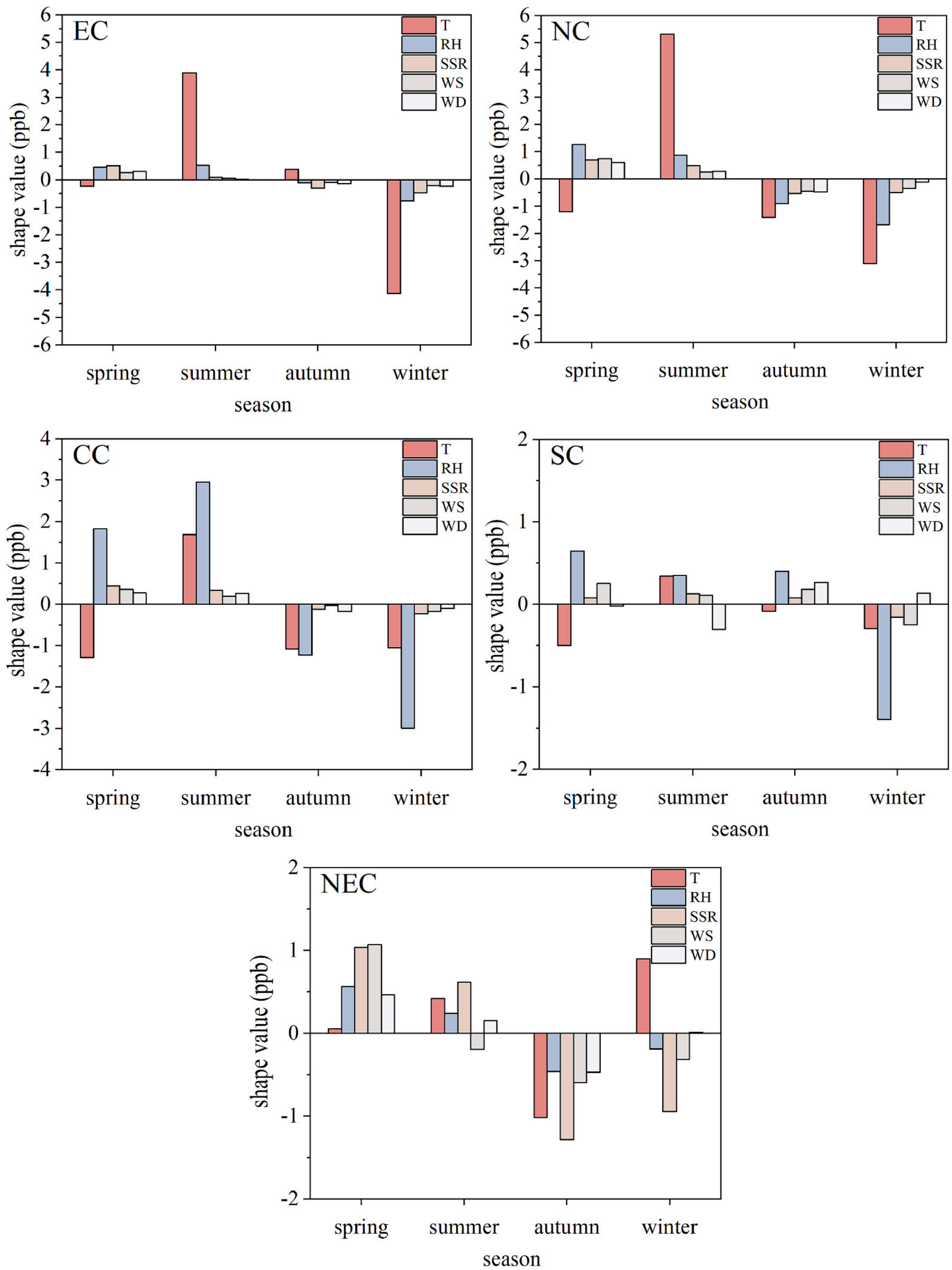

Fig. 6. Contributions of meteorological factors to O_{3_RBG} in different regions in four seasons. T represents surface temperature, RH represents relative humidity, SSR represents the amount of radiation reaching the surface, WS represents wind speed and WD represents wind direction. The Shap value represents the contribution of meteorological factors obtained from the Shapley additive explanations to O_{3_RBG}.

2.2. Study domain

Fig. 1a presents the distributions of seven regions discussed in this study, including Northeastern China (NEC), North China (NC), East China (EC), Southern China (SC), Central China (CC), Northwestern China (NWC), and Southeast China (SWC). Detailed information about the geographic regions can be found in Table S1. Fig. 1b classifies the regions into three groups according to the topographies, climate zones, and emission sources. The NC, south EC, and southern NEC regions are in the eastern plain and hilly areas in eastern China (EPH region). This region has intensive human activities, and the NO*x* and VOCs emissions are dominated by anthropogenic sources. The CC, SC, northern NEC, and northern NEC regions are in the high-altitude area in central China (HAA region). This region is composed of mountains and plateaus, and the emissions mainly come from natural sources. The western parts of the NWC and SWC regions are mainly arid areas with low vegetation coverage in western China (ALV region).

2.3. Model configuration

The Weather Research and Forecasting model (WRF, v4.3) (Powers et al., 2017) coupled with the most updated Community Multiscale Air Quality model (CMAQ, v5.3.2) (Appel et al., 2021) system is applied to estimate the O_{3_RBG} and O_{3_LC} concentrations of surface O_3 in China. The

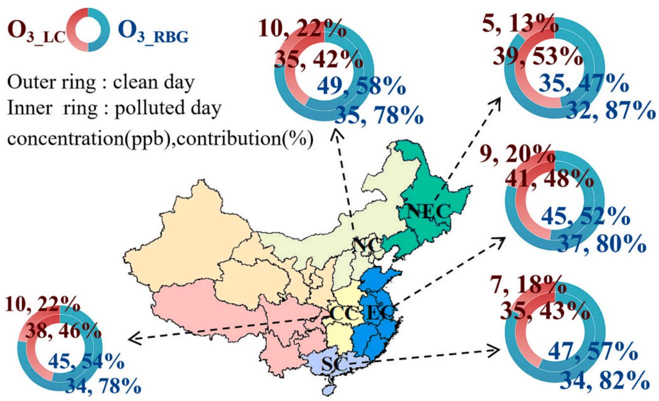

Fig. 7. O_{3_RBG} and O_{3_LC} concentrations in different regions (except NWC and SWC) on polluted days and clean days. The outer circle represents clean days, and the inner circle represents polluted days. Blue color represents O_{3_RBG}, and orange-red color represents O_{3_LC}. The number on the left of the comma indicates the concentration, and the number on the right indicates the contribution to O_3.

WRF model is driven by the National Centers for Environmental Prediction National Center for Atmospheric Research Reanalysis data (https://rda.ucar.edu/datasets/ds083.2), with a spatial resolution of 1° × 1° and a temporal resolution of 6 h. The boundary conditions are updated every 6 h to provide the WRF model with boundary fields. In terms of the operating mechanism, the WRF model simulation utilizes the global Rapid Radiative Transfer Model long wave scheme (Bae et al., 2016), the Goddard shortwave radiation scheme (Tao et al., 2016), the Yonsei University Planetary Boundary Layer scheme (Xie and Fung, 2014), the Noah Multi-Physics land surface model (Zhang et al., 2016a) and the Purdue-Lin microphysics scheme (Mielikainen et al., 2014). The CMAQ model is a widely used CTM model in air pollution research (Simon et al., 2012; Zhang et al., 2016b). The CB06 gas phase chemistry mechanism, AERO06 aerosol chemistry (Luecken et al., 2019), and M3DRY dry deposition mechanism (Appel et al., 2021) are adopted within the modeling system. The Whole-Atmosphere Community Climate Model (WACCM) provides the boundary conditions for the CMAQ model at six-hour intervals. The simulation included a 15-day spin-up period.

The model domain covers China and the surrounding area (Fig. 1), with a spatial resolution of 36 km × 36 km. The WRF model extends 6 grid cells further on each side of the CMAQ model. We simulated the entire year of 2020 and demonstrated the results of the four seasons separately: spring (March, April, May), summer (June, July, August), autumn (September, October, November), and winter (January, February, December). For most regions of China, spring and summer are the warm seasons with the highest temperatures in summer. The warm season in the SC is autumn due to its proximity to the equator (Zhou and Huang, 2014).

The emission inputs of the CMAQ model include both anthropogenic and natural emissions. The anthropogenic emission inventory within China is based on the Multi-resolution Emission Inventory of China (MEIC) for the year 2018 with a spatial resolution of 0.25° × 0.25° (Kang et al., 2016). It provides anthropogenic emissions from industry, power plants, agriculture, mobile, and residence. Emissions from anthropogenic sources outside China are from the Emission Database for Global Atmospheric Research (EDGAR) maintained by the European Commission (Olivier et al., 1994). The SNO*x* and BVOCs emissions are estimated by the Model of Emissions of Gases and Aerosols from Nature (MEGAN, v3.1) (Guenther, 2007). The emissions from wildfires are derived from the high spatiotemporal resolution fire inventory from NCAR (FINN) (Wiedinmyer et al., 2011). The other emission inputs are obtained from the online calculations of the CMAQ model. LNO*x* is determined by empirical relationships between lightning and convective precipitation, cloud layers, and others (Kang et al., 2019). The dependence of O_3 on sea salt halogens relies on the Sea Spray Emissions Module (Kang et al., 2019). Meanwhile, stratospheric transport is derived based on the correlation between potential vorticity and stratospheric intrusion O_3 (Xing et al., 2016).

We obtained the model predicted O_3 (O_{3_SIM}), O_{3_RBG} (O_{3_SRBG}), and O_{3_LC} (O_{3_SLC}) concentrations by using the CTM-BFM method. We setup two scenarios, including the Base case and Control case. In the base case, we used the abovementioned emission inventories for anthropogenic and natural emissions. In the control case, we kept the same set-up as the base case but excluded the anthropogenic emissions of China. O_{3_SRBG} is calculated by the control case. O_{3_SLC} is calculated by the difference between the base case and the control case.

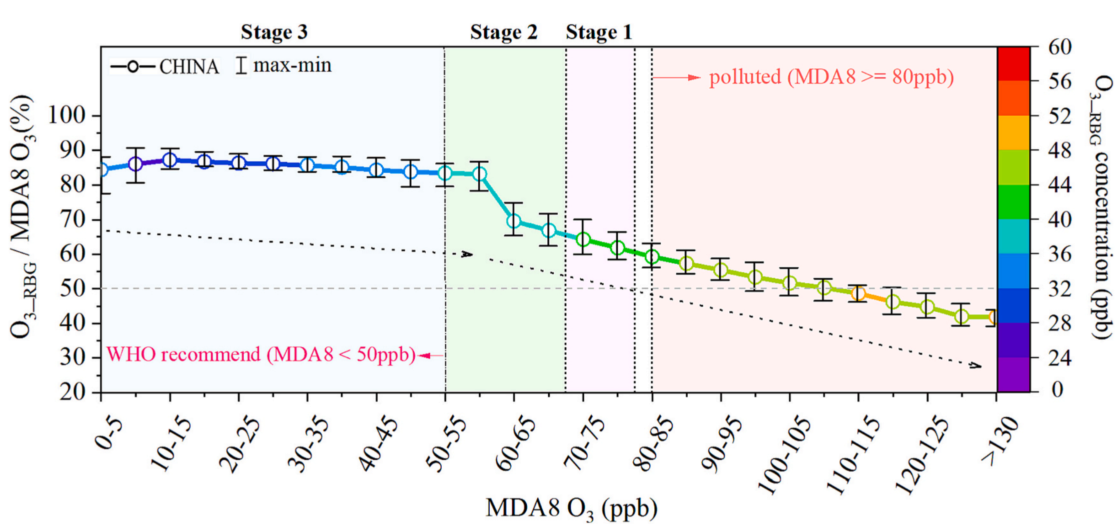

Fig. 8. The variations of O_{3_RBG} in different MDA8 O_3 ranges. The y-axis represents the proportions of O_{3_RBG} in MDA8 O_3. The x-axis represents different MDA8 O_3 ranges. The dots line represents the trends of O_{3_RBG} for China and error bars represents the maximum and minimum values of the seven geographical regions. The colors of the dots line indicate the concentrations of O_{3_RBG}. The pink background represents MDA8 $O_3 \geq 80$ ppb, purple background represents stage1 (67 ppb < MDA8 O_3 < 77 ppb), purple background represents stage1 (67 ppb < MDA8 O_3 < 77 ppb), green background represents stage2 (50 ppb < MDA8 $O_3 \leq 67$ ppb) , blue background represents stage3 (MDA8 $O_3 \leq 50$ ppb).

2.4. MLR model

The MLR model has been widely used in the field of atmospheric pollution forecasting and analysis (Han et al., 2020; Hsu et al., 2022; Qian et al., 2022; Skipper et al., 2021). This method establishes a relationship between the dependent and independent variables, deriving corresponding regression coefficients (α) acting on the independent variables for a better fit of the dependent variable. This is accomplished through the least squares method, which minimizes the total sum of squared errors to find the optimal function and solve for α.

O_{3_OBS} are composed of O_{3_RBG} and O_{3_LC} (Eq. (1)). We employed the CTM-BFM method to simulate the O_{3_RBG} (denoted as O_{3_SRBG}) and O_{3_LC} (denoted as O_{3_SLC}) concentrations. These two values are deviated from the true value of O_{3_RGB} and O_{3_LC} due to bias in CTM and the BFM approach. We then establish the MLR model, where O_{3_SRBG} and O_{3_SLC} are constrained by O_{3_OBS} (Eqs. (2)–(3)). As mentioned earlier, α, resolved by MLR, serves as an indicator of the degree to which simulations are constrained by observations. The MLR model is described as follows:

$$O_{3\_OBS} = O_{3\_RBG} + O_{3\_LC} \tag{1}$$

$$O_{3\_RBG} = O_{3\_SRBG} \times \alpha_{RBG}\ (X, Y, Z) \tag{2}$$

$$O_{3\_LC} = O_{3\_SLC} \times \alpha_{LC}\ (X, Y, Z) \tag{3}$$

where α_{RBG} (α_{LC}) represent α of O_{3_SRBG} (O_{3_SLC}).

The α_{RBG} and α_{LC} values are affected by the geographic information (De Bock et al., 2014; Yan et al., 2020). In this study, we used the standardized longitude (X), latitude (Y), and altitude (Z) to improve the MLR performance and explain the deviation between simulation and observation as shown in Eqs. (4)–(5).

$$\alpha_{RBG}\ (X, Y, Z) = \alpha_{0,RBG} + \alpha_{X,RBG} \times X + \alpha_{Y,RBG} \times Y + \alpha_{Z,RBG} \times Z \tag{4}$$

$$\alpha_{LC}\ (X, Y, Z) = \alpha_{0,LC} + \alpha_{X,LC} \times X + \alpha_{Y,LC} \times Y + \alpha_{Z,LC} \times Z \tag{5}$$

The MLR model solved the α values on the right side of Eqs. (4)–(5). Then, Eqs. (4)–(5) are substituted into Eqs. (2)–(3) to obtain the α_{RBG} and α_{LC} values. Each CTM grid has different α values based on X, Y, and Z information. Simultaneously, we obtain O_{3_SRBG} (O_{3_SLC}) constrained by O_{3_OBS} and consider them as our assessments for O_{3_RBG} (O_{3_LC}).

3. Results and discussion

3.1. MLR improvements over CMAQ

Fig. 2a, b, c demonstrates the performance of the WRF-CMAQ model in simulating the daily O_3 concentrations. The overall performance of the WRF model is acceptable, with slight underestimation in temperature, wind speed, and slight overestimation in the relative humidity (detailed information in Table S2). The CMAQ model succeeded in capturing the distribution of MDA8 O_3 in China (Fig. S1) but slightly overestimated the concentrations (Fig. 2a). The Correlation efficient (R) was 0.66, which is overall comparable or better than previous studies (Kuo and Fu, 2023). The normalized mean bias (NMB) and normalized mean error (NME) values were 25 % and 37 %, respectively and have both exceeded the benchmark by Emery et al. (2017) (Fig. 2b–c). Evaluations in different regions (Table S3) also indicate general overestimations of the O_3 concentrations over the whole of China. The uncertainty of CMAQ O_3 modeling in the Chinese region are common. Even within the same study (Kuo and Fu, 2023), the simulation's R in same region may vary noticeably due to differences in simulation time period (0.4–0.8). Shi et al. (2021) and Xing et al. (2017) conducted simulations with different meteorological scenarios or for different regions nationwide. Their NMB exhibit considerable variations across different regions or months (−50 % to 250 %, averaging 33 % and 32 %). The overestimation of O_3 using CTM is mainly attributed to inventory input, chemical mechanisms, and boundary conditions used (Fink et al., 2023; Hou et al., 2022b; Xiong et al., 2023). The anthropogenic emission inventory (MEIC) we utilized employed a bottom-up approach to calculate emissions of various atmospheric species. However, this approach often relies on the accuracy of statistical data and is prone to overlooking differences between cities, leading to disparities between predicted emissions and actual emissions (Saikawa et al., 2017; Wu et al., 2021). The gas chemical mechanism employed is based on SAPRC07, released in 2007, lacking some peroxyl radical and aromatic hydrocarbon reactions that could impact O_3 simulation. Additionally, the chemical mechanism lacks numerous halogen reactions, and halogen reactions have a significant influence on OH and O_3 production (Fan and Li, 2023; Yi et al., 2023).

The MLR model performed an overall improvement on the overestimation of MDA8 O_3 by the WRF-CMAQ model (Fig. 2a). The MLR model predicted an average 9 ppb lower O_3 values than the WRF-CMAQ model and reduced the mean bias (MB) from 10 ppb to 3 ppb (Fig. 2b). The MLR succeeded in providing a closer estimation to the observed MDA8 O_3 concentrations than the WRF-CMAQ model for all Chinese regions (Fig. 2a–c). In particular, the MLR model reduced the NMB and NME values of all regions to levels that were below the criterion standard (15 %). The improvements were most significant in the CC, SC, and NEC regions, followed by the NC and EC regions. The WRF-CMAQ performances were also improved in the NWC and SWC regions. However, we found large uncertainties in the interpretation of the results in this region due to the insufficient number of observational sites (Fig. 1a). Therefore, we retained the result for this region but excluded it in the following discussion. More details about α and MLR model performance can be found in Table S4-S5.

Fig. 2d, e, f compares the spatial distributions of surface MDA8 O_3, O_{3_RBG}, and O_{3_LC} simulated by the WRF-CMAQ model and those adjusted by MLR. The adjustments on the O_{3_RBG} concentrations ranged between 4–20 ppb, especially in the HAA region. The changes in the O_{3_LC} concentrations were <4 ppb and mainly took place in the ALV region where there remain large uncertainties as mentioned above. One possible reason is the overestimation of O_3 formation of the HAA region caused by model underestimation in the cloud optical depth and underestimation of O_3 removal caused by underestimation of dry deposition (Ye et al., 2022). Since the CTM predicted higher O_{3_RBG} than O_{3_LC}, the adjustments by observations are higher on O_{3_RBG} than O_{3_LC}. Another possible reason points to the non-linear response of O_3 to its precursors. Previous studies have indicated that when applying BFM to separate the contribution of natural and anthropogenic emissions, the sum of naturally sourced O_3 and anthropogenic sourced O_3 would be higher than the total-undifferentiated O_3 concentrations, caused by the nonlinear response of O_3 concentrations to changes in NO*x* and VOCs emissions (Fang et al., 2020; Kwok et al., 2015). In the BFM approach, after removing ANO*x* emissions in the control case, the whole research domain would be lack of ANO*x* titration reaction resulting in an overestimation of O_{3_RBG} (Chen et al., 2022). Thus, the influence is more significant on NO*x*-limited regions than VOC-limited regions. According to Ren et al. (2022), most Chinese regions except the south NC region are NO*x*-limited and the south NC region is VOC-limited in the year 2020. This could well explain the spatial distribution of the adjustment in O_{3_RBG} (Fig. 2d).

We compared our results with previous studies by using statistical methods and CTM methods. Lu et al. (2019) used the GEOS-CHEM model and BFM approach to estimate the O_{3_RBG} in China for year 2016 and 2017. Our results were 4–5 ppb lower than theirs during May–August, and 6–7 ppb lower during March–April and September–October. Wang et al. (2022a) used the MLR-PCA- Texas Commission on Environmental Quality (TCEQ) system to estimate the O_{3_RBG} in Shandong Province for years 2018–2020. Our result (38 ppb) for year 2020 is slightly lower than theirs (41.5 ppb for the three years average), but rather comparable. Chen et al. (2022) estimate the O_{3_RBG} by estimating the stable O_3 concentrations at a certain temperature range. Our results are 10–20 ppb lower than theirs during December–February and 3–10 ppb lower during May–August. Whether comparing with the O_3 background concentrations obtained solely through the use of BFM in our study, or with findings from other studies, the O_3 background concentrations derived from MLR-BFM in our study are consistently lower. It is worth noting that the differences in research time period and inputs will inevitably affect the results. However, comparing with others can still serve as a valid reference and is necessary, especially when we focus on the final O_{3_RBG} obtained.

3.2. Spatial distribution of O_{3_RBG} and its contribution to total O_3

Fig. 3 summarizes the concentrations of O_{3_RBG} and O_{3_LC} in seven regions of China. Fig. 4 shows the spatial variations of O_3 and O_{3_RBG} in different seasons. The O_{3_RBG} ranged between 22–45 ppb and averaged at 35 ± 4 ppb in China for the year 2020. Compared to the spatial distribution of O_3 (Fig. 4a), distribution of O_{3_RBG} is relatively homogenous (Fig. 4b). The EC region has the highest O_{3_RBG} concentrations (37 ppb), followed by the NC (36 ppb), CC (35 ppb), SC (34 ppb) regions and the other regions (32–33 ppb). The contribution of O_{3_RBG} to total O_3 ranged between 71–92 % and averaged at 81 ± 5 % over China. The HAA region has a 10 % higher proportion of O_{3_RBG} in MDA8 O_3 (85%) than the EPH region (75 %) (Fig. 4c).

The HAA region has generally higher O_{3_RBG} concentrations than the EPH region. Research suggests that factors such as the elevated inversion layer and the influence of pollutants' mesoscale circulation at higher altitudes contribute to elevated O_3 concentrations in mountainous areas (Guo et al., 2013). In addition, stratosphere-troposphere intrusion of O_3 in western and northwestern China at higher altitudes could induce about 5–10 ppb of O_3 during lightning-active months (Lu et al., 2019; Roy et al., 2017; Xu et al., 2016). Due to lower anthropogenic VOCs (AVOCs) emissions in the HAA region, this region has a high proportion of O_{3_RBG}.

For the EPH region, the large emissions of SNO*x* (and soil HONO) are one of the reasons for high O_{3_RBG} in the southern of NC and northern of EC regions during summer (Lu et al., 2019; Lyu et al., 2022; Xue et al., 2021; Huang et al., 2023) (Fig. 4i). The concentrations in coastal region (EC and NC) are about 1–4 ppb higher than that in inland region, which may reflect the contribution of marine background O_3 (Lam et al., 2001; Wang et al., 2022a).

3.3. Driving factors of seasonal variations of O_{3_RBG}

Meteorology (solar radiation, temperature, precipitation, etc.) and natural emissions are the main drivers of the seasonal distributions of O_{3_RBG} in China. To get insights into the contributions of meteorological factors and natural emissions to O_{3_RBG}, we adopted meteorological standardization, random forest, and Shapley additive explanations to interpret the driving forces of O_{3_RBG}. We derived hourly contributions of meteorology (O_{3_RBG} concentration of weather contribution, O_{3_wc}) and natural emissions (O_{3_RBG} concentration of removing meteorology, O_{3_rmw}) to O_{3_RBG} (Fig. 5). Additionally, based on previous studies employing this method, we identified the meteorological factors that have a relatively significant impact on O_3 and determined their contributions (Shap value from Shapley additive explanations) to O_{3_RBG} (Fig. 6). More details about our machine learning method can be found in Xue et al. (2023), Hou et al. (2022a), and Grange et al. (2018). Model performance evaluation about our machine learning methods is shown in Table S6.

From the results, it is evident that O_{3_rmw} contribute more to O_{3_RBG} on average than O_{3_wc}, a commonality across all regions and seasons. The extreme values of O_{3_wc}'s contribution differ more significantly than O_{3_rmw}'s, with instances of negative contributions, indicating substantial fluctuations in meteorological contributions. In spring (Fig. 5a), meteorological conditions favor O_{3_RBG} production (Feng and Wang, 2020), and O_{3_wc}'s overall average contribution is 2 ppb (1.4 ppb to 5 ppb). The relatively high emissions of BVOCs and SNOx (Dai et al., 2018; Mohanty and Panda, 2011; Ruan et al., 2004) result in O_{3_rmw} being in a higher concentration range (36–39 ppb). With the arrival of summer (Fig. 5b), O_{3_rmw} in most areas (except the NEC region and SC region, discussed later) enters a period of highest concentration (37–40 ppb), associated with further enhanced emissions of BVOCs and SNOx. O_{3_wc} in heavily polluted areas like the NC region and EC region also reach peaking concentrations (4.6 ppb, 7.7 ppb). In the NEC region, O_{3_rmw} contributes more in spring, aligning with the fact that its O_{3_RBG} and MDA8 O_3 are highest in spring (Shang et al., 2023). In the SC region, autumn has the highest emissions of BVOCs and SNOx, hence the highest autumn O_{3_rmw} (Fig. 5, c). Additionally, SC is the only region where O_{3_wc} is positive in autumn (1.03 ppb), as the SC region experiences weather conditions in autumn conducive to O_3 production. For other regions, both O_{3_rmw} and O_{3_wc} contributions are lower in autumn and winter compared to spring and summer, atribute to reduced emissions of BVOCs and SNO_x and meteorological conditions less favorable for O_3 production. In winter (Fig. 5d), radiation hits its yearly minimum, temperatures drop, and wind speeds increase. For most regions in China, O_{3_wc} contributions reach their yearly minimum.

Fig. 6 illustrates the contributions of various meteorological factors to O_{3_RBG} in different regions in different seasons. Regarding the contribution of meteorology to O_{3_RBG}, it's noteworthy that there are apparent negative contributions. Therefore, we additionally take the absolute values of meteorological factors' contributions to O_{3_RBG} in Fig. S2 to illustrate the influencing capacity of meteorological factors on O_{3_RBG}. In spring, humidity has the highest contribution in the CC, NC, and SC regions (1.3–1.9 ppb), and its absolute impact is also higher (30 %–40 %). The EC region exhibits a larger contribution from radiation (0.52 ppb), with relative humidity ranking second (0.47 ppb), but the absolute impact of temperature is the highest (29 %). For the NEC region, different from other regions, both radiation and wind speed contribute more (both 1 ppb). In summer, temperature dominates the contributions in two O_3 heavily polluted regions, the EC region and NC region (3.8 ppb and 5.3 ppb), with absolute contributions of 46 % and 52 %, emphasizing the impact of temperature and hot weather on heavily polluted areas. The CC region is also more influenced by humidity (2.9 ppb), but the contribution of temperature shifts from −1.2 ppb in spring to a positive contribution of 1.7 ppb. In autumn, temperature continues to contribute positively in the EC region but decreases to 0.38 ppb. Humidity becomes the more influential meteorological factor in the EC region (45 %). In the northern latitudes, where temperatures are colder in the NC region and CC region, temperature becomes a negative contributor (−1.4 ppb and − 1.07 ppb), with the highest absolute impact (34 % and 36 %). In winter, the NC region is still most significantly influenced by temperature (43 %), contributing −4.1 ppb. In the EC region, the contribution from temperature is −4.13 ppb, dominating the meteorological factors, with an absolute impact percentage of 62 %. Overall, for heavily polluted areas like the NC region and EC region, temperature plays a predominant role in influencing O_3, while humidity has a greater impact in the SC region. For other regions, the CC region is mainly influenced by humidity, and the NEC region is significantly influenced by temperature, radiation, and wind speed.

3.4. Contributions at different O_3 levels

Although China has implemented ambitious emission reduction plans for anthropogenic VOCs and NO_x over the past decade, the annual variation in O_3 concentration remains fluctuating without a clear downward trend. We analyze the forms of O_3 pollution in China from the perspective of O_{3_RBG} and O_{3_LC} contributions. Fig. 7 shows the average O_{3_RBG} and O_{3_LC} on clean days (MDA8 $O_3 < 80$ ppb) and polluted days (MDA8 $O_3 \geq 80$ ppb) for different regions. On clean days, the average O_{3_RBG} concentration is around 34 ppb and contributes 81 % to total O_3. On polluted days, the average O_{3_RBG} value increased to 45 ppb but the contribution decreased to 55 %, indicating the relatively higher contributions from anthropogenic precursor emissions. There is a significant increase in the proportion of O_{3_LC} on pollution days in all regions (an average increase of 250 % compared to clean days). In NC and SC regions, the O_{3_RBG} (49 ppb, 47 ppb) on polluted days is higher compared to other areas, corresponding to elevated emissions of biogenic precursors in these two regions. It is worth noting that the NEC region has the highest increase in O_{3_LC} contribution on pollution days. This may be due to the fact that, unlike other regions, the contribution of external O_3 in the warm season of NEC exceeds 60 %, the concentration of precursor substances from local anthropogenic sources is lower, and the ability of NO to titrate O_3 is weak (Fang et al., 2021). Detailed assessments for each province can be found in Table S7-S9.

To further analyze the relative contributions of O_{3_RBG} and O_{3_LC} to environmental O_3 pollution control policies, we sampled MDA8 O_3 every 5 ppb and tracked the changes in O_{3_RBG} and O_{3_LC} (Fig. 8). Over the past decade, China's MDA8 O_3 90th percentile mainly remained within the Stage 1 range (67–77 ppb, Fig. 6, Stage 1). We found that the substantial contribution of O_{3_LC} on polluted days leads to extremely high concentrations of MDA8 O_3, supporting the current Chinese strategy of reducing peak O_3 concentrations. Additionally, O_{3_LC} constitutes 35–40 % of MDA8 O_3, indicating that there is still a considerable amount of O_{3_LC} that can be reduced. This supports the Chinese government's view of strengthening the reduction of anthropogenic VOCs and NO_x to reduce O_3 concentrations. However, it is worth noting that in Stage 1, the proportion of O_{3_RBG} has already reached 60–65 %. This implies that if O_3 concentrations are reduced solely by decreasing anthropogenic VOCs and NOx, while neglecting the contribution of O_{3_RBG}, the effectiveness may be reduced by more than half. Stage 2 represents the next target for China after escaping the O_3 concentration range from Stage 1. Since the Chinese government has not clearly specified the expected range of future O_3 concentrations, we adopted the World Health Organization's recommended 50 ppb as the target, considered an acceptable O_3 concentration. We defined the range of 50–67 ppb as Stage 2 (Fig. 8, Stage 2), representing the O_3 concentration reduction that China still needs to achieve. To reach a pollution-free level, China needs to reduce the O_3 concentration by at least 17 ppb. In this process, the proportion of O_{3_RBG} will increase from 66 % to 73 %. This emphasizes the importance of O_{3_RBG} and underscores the necessity of strengthening inter-regional joint prevention and control measures to transition from Stage 2 to Stage 3 (below 50 ppb, Fig. 8, Stage 3) and achieve the goal.

3.5. Uncertainty analysis

There are two primary factors contributing to the uncertainties in estimating $O_{3\_RBG.}$ The first is related to uncertainties of MLR. The choice of independent variables affects the way the dependent variable is interpreted. In this study, we standardized the independent variables into consistent concentration units and estimated the impact of O_3 background concentrations, local photochemical reactions, standardized normalized longitude, standardized normalized latitude, and standardized normalized altitude on observed O_3. However, it is worth noting that O_3 background concentrations and local photochemical reactions predominantly account for the influences, which have been confirmed by others as well (Skipper et al., 2021). Therefore, the inclusion of additional independent variables has minimal overall impact on the relationship between total O_3 and O_3 background concentrations and local photochemical reactions. On the other hand, The training dataset also influences the results of MLR, similar to machine learning, where a large and valid dataset leads to more convincing and satisfactory outcomes (Shang et al., 2023). This is also why we excluded data from the ALV region, as the available training data is too limited compared to the extensive area.

4. Conclusions

In this study, we applied the MLR method to constrain model predicted O_3 and O_{3_RBG} from CTM with site observations of O_3. There has not been a report using this method to assess China's O_3 background concentrations. Our results demonstrate that this approach has significant improvement on the CTM model performance on predicting O_3 over the whole of China. We estimated the average O_{3_RBG} in China to be 35 $\pm$ 4 ppb, accounting for 81 $\pm$ 5 % of MDA8 O_3. The O_{3_RBG} concentrations are higher in warm seasons (spring 39 ppb, summer 38 ppb) than in cold seasons (winter 31 ppb, autumn 30 ppb). Their contributions to total O_3 are slightly lower in the warm seasons (78 %) than cold seasons (83 %). Natural emissions contribute (31–40 ppb) more significantly than meteorology to O_{3_RBG} in various regions and seasons. Meteorological contributions exhibit greater fluctuations, with negative contributions, reaching a seasonal average of 4.6–7.7 ppb during the summer in heavily polluted areas (EC and NC regions). Temperature and relative humidity emerge as the two predominant meteorological factors with the highest impact in urban areas, with their contributions ranging from 30 % to 62 %.

We further investigated the role of O_{3_RBG} in controlling O_3 pollution. The average O_{3_RBG} concentration is 34 ppb on clean days (daily MDA8 $O_3 < 80$ ppb) and contributes 81 % to total O_3. The value increased to 45 ppb on polluted days (daily MDA8 $O_3 > 80$ ppb) and contributes 55 % to total O_3. The contribution of O_{3_LC} on pollution days over 45 %, supporting the current Chinese policy's goal of reducing O_3 peak concentrations by minimizing anthropogenic precursor emissions. Within the O_3 concentration 90th percentile range of the past decade, O_{3_LC} has contributed 35–40 % to MDA8 O_3. This supports the Chinese government's view of strengthening the reduction of anthropogenic precursor emissions to lower O_3 concentrations. However, O_{3_RBG}'s contribution to MDA8 O_3 already exceeds half and is expected to rise to 73 % with further reduction in anthropogenic precursor emissions, reaching the WHO-recommended target of 50 ppb. Therefore, there is a critical need to emphasize the importance of including O_{3_RBG} in policies, an aspect currently missing, and to prioritize regional joint prevention and control measures.

CRediT authorship contribution statement

Zhixu Sun: Conceptualization, Data curation, Formal analysis, Methodology, Software, Visualization, Writing – original draft. **Jiani Tan:** Formal analysis, Investigation, Methodology, Validation, Writing – review & editing. **Fangting Wang:** Formal analysis. **Rui Li:** Conceptualization, Funding acquisition, Investigation, Methodology, Project administration, Resources, Supervision, Writing – review & editing. **Xinxin Zhang:** Formal analysis. **Jiaqiang Liao:** Formal analysis. **Yangjun Wang:** Conceptualization, Methodology. **Ling Huang:** Conceptualization, Investigation. **Kun Zhang:** Formal analysis, Methodology. **Joshua S. Fu:** Methodology, Writing – review & editing. **Li Li:** Conceptualization, Funding acquisition, Investigation, Methodology, Project administration, Resources, Supervision, Writing – review & editing.

Declaration of competing interest

The authors declare that they have no conflict of interest.

Data availability

Data will be made available on request.

Acknowledgements

This study is financially supported by the Shanghai Municipal Bureau of Ecology and Environment Fund Project ([2022]37) and the

National Natural Science Foundation of China (nos. 42075144 and 42375102).

Appendix A. Supplementary data

Supplementary data to this article can be found online at https://doi.org/10.1016/j.scitotenv.2023.169411.

References

Appel, K.W., Bash, J.O., Fahey, K.M., Foley, K.M., Gilliam, R.C., Hogrefe, C., Hutzell, W.T., Kang, D.W., Mathur, R., Murphy, B.N., Napelenok, S.L., Nolte, C.G., Pleim, J.E., Pouliot, G.A., Pye, H.O.T., Ran, L.M., Roselle, S.J., Sarwar, G., Schwede, D.B., Sidi, F.I., Spero, T.L., Wong, D.C., 2021. The community multiscale air quality (CMAQ) model versions 5.3 and 5.3.1: system updates and evaluation. Geosci. Model Dev. 14, 2867–2897.

Atherton, C.S., Sillman, S., Walton, J., 1996. Three-dimensional global modeling studies of the transport and photochemistry over the North Atlantic Ocean. J. Geophys. Res.-Atmos. 101, 29289–29304.

Bae, S.Y., Hong, S.Y., Lim, K.S.S., 2016. Coupling WRF double-moment 6-class microphysics schemes to RRTMG radiation scheme in weather research forecasting model. Adv. Meteorol. 2016.

Barnes, P., Robson, T., Zepp, R., Bornman, J., Jansen, M., Ossola, R., Wang, Q.-W., Robinson, S., Foereid, B., Klekociuk, A., 2023. Interactive effects of changes in UV radiation and climate on terrestrial ecosystems, biogeochemical cycles, and feedbacks to the climate system. Photochem. Photobiol. Sci. 1–43.

Chen, W.H., Guenther, A.B., Shao, M., Yuan, B., Jia, S.G., Mao, J.Y., Yan, F.H., Krishnan, P., Wang, X.M., 2022. Assessment of background ozone concentrations in China and implications for using region-specific volatile organic compounds emission abatement to mitigate air pollution. Environ. Pollut. 305.

Cheng, L., Wang, S., Gong, Z., Yang, Q., Wang, Y., 2017. Spatial and seasonal variation and regionalization of ozone concentrations in China. China Environ. Sci. 37, 4003–4012.

Dai, Y., Wang, H., Li, A., Zhu, Y., Wang, X., Fang, Z., Xu, X., 2018. Dynamical pattern of soil microbial biomass and its response to nitrogen and phosphorus additions in a subtropical evergreen broad-leaved forest. J. Ecol. Environ. Sci. 27, 1395–1404.

De Bock, V., De Backer, H., Van Malderen, R., Mangold, A., Delcloo, A., 2014. Relations between erythemal UV dose, global solar radiation, total ozone column and aerosol optical depth at Uccle, Belgium. Atmos. Chem. Phys. 14, 12251–12270.

Emery, C., Liu, Z., Russell, A.G., Odman, M.T., Yarwood, G., Kumar, N., 2017. Recommendations on statistics and benchmarks to assess photochemical model performance. J. Air Waste Manage. Assoc. 67, 582–598.

Fan, S.D., Li, Y., 2023. Potential deterioration of ozone pollution in coastal areas caused by marine- emitted halogens: a case study in the Guangdong-Hong Kong-Macao Greater Bay Area. Sci. Total Environ. 860.

Fang, C.S., Gao, H.B., Li, Z.Q., Wang, J., 2021. Regional air pollutant characteristics and health risk assessment of large cities in Northeast China. Atmosphere 12.

Fang, T., Zhu, Y., Jang, J., Wang, S., Xing, J., Chiang, P.-C., Fan, S., You, Z., Li, J., 2020. Real-time source contribution analysis of ambient ozone using an enhanced meta-modeling approach over the Pearl River Delta Region of China. J. Environ. Manag. 268, 110650.

Feng, F., Wang, K., 2020. High Spatial Resolution (10 km) Surface Solar Radiation Dataset With by Merging Sunshine Hours Over China China (1983–2017). Beijing, China, National Tibetan Plateau Data Center.

Fink, L., Karl, M., Matthias, V., Oppo, S., Kranenburg, R., Kuenen, J., Moldanova, J., Jutterström, S., Jalkanen, J.P., Majamäki, E., 2023. Potential impact of shipping on air pollution in the Mediterranean region - a multimodel evaluation: comparison of photooxidants NO2 and O3. Atmos. Chem. Phys. 23, 1825–1862.

Grange, S.K., Carslaw, D.C., Lewis, A.C., Boleti, E., Hueglin, C., 2018. Random forest meteorological normalisation models for Swiss PM10 trend analysis. Atmos. Chem. Phys. 18, 6223–6239.

Gu, X., Wang, T., Li, C., 2022. Elevated ozone decreases the multifunctionality of belowground ecosystems. Glob. Chang. Biol. 29, 890–908.

Guenther, A., 2007. Estimates of global terrestrial isoprene emissions using MEGAN (model of emissions of gases and aerosols from nature) (vol 6, pg 3181, 2006). Atmos. Chem. Phys. 7, 4327.

Guo, H., Ling, Z.H., Cheung, K., Jiang, F., Wang, D.W., Simpson, I.J., Barletta, B., Meinardi, S., Wang, T.J., Wang, X.M., Saunders, S.M., Blake, D.R., 2013. Characterization of photochemical pollution at different elevations in mountainous areas in Hong Kong. Atmos. Chem. Phys. 13, 3881–3898.

Guo, J., Zhang, X., Gao, Y., Wang, Z., Zhang, M., Xue, W., Herrmann, H., Brasseur, G.P., Wang, T., Wang, Z., 2023. Evolution of ozone pollution in China: what track will it follow? Environ. Sci. Technol. 57, 109–117.

Han, H., Liu, J.E., Shu, L., Wang, T.J., Yuan, H.L., 2020. Local and synoptic meteorological influences on daily variability in summertime surface ozone in eastern China. Atmos. Chem. Phys. 20, 203–222.

Hong, X., Chen, Z., 2020. Simulation study on typical ozone pollution process in the southeast coast of China in spring. Environ. Sci. Technol. 43, 105–114.

Hou, L., Dai, Q., Song, C., Liu, B., Guo, F., Dai, T., Li, L., Liu, B., Bi, X., Zhang, Y., Feng, Y., 2022a. Revealing drivers of haze pollution by explainable machine learning. Environ. Sci. Technol. Lett. 9, 112–119.

Hou, T.Y., Yu, S.C., Jiang, Y.P., Chen, X., Zhang, Y.B., Li, M.Y., Li, Z., Song, Z., Li, P.F., Chen, J.M., Zhang, X.Y., 2022b. Impacts of chemical initial conditions in the WRF-CMAQ model on the ozone forecasts in eastern China. Aerosol Air Qual. Res. 22.

Hsu, C.Y., Chang, Y.T., Lin, C.J., 2022. How a winding-down oil refinery park impacts air quality nearby? Environ. Int. 169.

Huang, J., Pan, X., Guo, X., Li, G., 2018. Health impact of China's air pollution prevention and control action plan: an analysis of national air quality monitoring and mortality data. Lancet Planet. Health 2, e313–e323.

Huang, L., Fang, J., Liao, J., Greg, Y., Chen, H., Wang, Y., Li, L., 2023. Insights into soil NO emissions and the contribution to surface ozone formation in China. EGUsphere 2023, 1–19.

Huang, Z.J., Zheng, J.Y., Ou, J.M., Zhong, Z.M., Wu, Y.Q., Shao, M., 2019. A feasible methodological framework for uncertainty analysis and diagnosis of atmospheric chemical transport models. Environ. Sci. Technol. 53, 3110–3118.

Kang, D., Foley, K.M., Mathur, R., Roselle, S.J., Pickering, K.E., Allen, D.J., 2019. Simulating lightning NO production in CMAQv5.2: performance evaluations. Geosci. Model Dev. 12, 4409–4424.

Kang, Y.N., Liu, M.X., Song, Y., Huang, X., Yao, H., Cai, X.H., Zhang, H.S., Kang, L., Liu, X.J., Yan, X.Y., He, H., Zhang, Q., Shao, M., Zhu, T., 2016. High-resolution ammonia emissions inventories in China from 1980 to 2012. Atmos. Chem. Phys. 16, 2043–2058.

Knowland, K.E., Doherty, R.M., Hodges, K.I., Ott, L.E., 2017. The influence of mid-latitude cyclones on European background surface ozone. Atmos. Chem. Phys. 17, 12421–12447.

Kuo, C.-P., Fu, J.S., 2023. Ozone response modeling to NOx and VOC emissions: examining machine learning models. Environ. Int. 176, 107969.

Kwok, R.H.F., Baker, K.R., Napelenok, S.L., Tonnesen, G.S., 2015. Photochemical grid model implementation and application of VOC, NOx, and O-3 source apportionment. Geosci. Model Dev. 8, 99–114.

Lam, K.S., Wang, T.J., Chan, L.Y., Wang, T., Harris, J., 2001. Flow patterns influencing the seasonal behavior of surface ozone and carbon monoxide at a coastal site near Hong Kong. Atmos. Environ. 35, 3121–3135.

Lelieveld, J., Evans, J.S., Fnais, M., Giannadaki, D., Pozzer, A., 2015. The contribution of outdoor air pollution sources to premature mortality on a global scale. Nature 525, 367.

Li, A., Zhou, Q., Xu, Q., 2021. Prospects for ozone pollution control in China: an epidemiological perspective. Environ. Pollut. 285, 117670.

Li, J.R., Kohno, N., Sakamoto, Y., Pham, H.G., Murano, K., Sato, K., Nakayama, T., Kajii, Y., 2022. Potential factors contributing to ozone production in AQUAS-Kyoto campaign in summer 2020: natural source-related missing OH reactivity and heterogeneous HO2/RO2 loss. Environ. Sci. Technol. 56, 12926–12936.

Li, N., He, Q.Y., Greenberg, J., Guenther, A., Li, J.Y., Cao, J.J., Wang, J., Liao, H., Wang, Q.Y., Zhang, Q., 2018. Impacts of biogenic and anthropogenic emissions on summertime ozone formation in the Guanzhong Basin, China. Atmos. Chem. Phys. 18, 7489–7507.

Li, Y., Lau, A.K.H., Fung, J.C.H., Zheng, J.Y., Zhong, L.J., Louie, P.K.K., 2012. Ozone source apportionment (OSAT) to differentiate local regional and super-regional source contributions in the Pearl River Delta region, China. J. Geophys. Res.-Atmos. 117.

Lu, X., Zhang, L., Chen, Y.F., Zhou, M., Zheng, B., Li, K., Liu, Y.M., Lin, J.T., Fu, T.M., Zhang, Q., 2019. Exploring 2016-2017 surface ozone pollution over China: source contributions and meteorological influences. Atmos. Chem. Phys. 19, 8339–8361.

Lu, X., Zhang, L., Wang, X., Gao, M., Li, K., Zhang, Y., Yue, X., Zhang, Y., 2020. Rapid increases in warm-season surface ozone and resulting health impact in China since 2013. Environ. Sci. Technol. Lett. 7, 240–247.

Luecken, D.J., Yarwood, G., Hutzell, W.T., 2019. Multipollutant modeling of ozone, reactive nitrogen and HAPs across the continental US with CMAQ-CB6. Atmos. Environ. 201, 62–72.

Lyu, X., Guo, H., Zou, Q., Li, K., Xiong, E., Zhou, B., Guo, P., Jiang, F., Tian, X., 2022. Evidence for reducing volatile organic compounds to improve air quality from concurrent observations and in situ simulations at 10 stations in Eastern China. Environ. Sci. Technol. 56, 15356–15364.

Mathur, R., Kang, D.W., Napelenok, S.L., Xing, J., Hogrefe, C., Sarwar, G., Itahashi, S., Henderson, B.H., 2022. How have divergent global emission trends influenced long-range transported ozone to North America? J. Geophys. Res.-Atmos. 127.

McDonald-Buller, E.C., Allen, D.T., Brown, N., Jacob, D.J., Jaffe, D., Kolb, C.E., Lefohn, A.S., Oltmans, S., Parrish, D.D., Yarwood, G., Zhang, L., 2011. Establishing policy relevant background (PRB) ozone concentrations in the United States. Environ. Sci. Technol. 45, 9484–9497.

Mielikainen, J., Huang, B.M., Huang, A.H.L., 2014. Initial results on computational performance of Intel Many Integrated Core (MIC) architecture: implementation of the weather and research forecasting (WRF) Purdue-Lin microphysics scheme. In: Conference on High-Performance Computing in Remote Sensing IV. Amsterdam, Netherlands.

Mohanty, R.B., Panda, T., 2011. Soil respiration and microbial population in a tropical deciduous forest soil of Orissa, India. Flora 206, 1040–1044.

Olivier, J.G.J., Bouwman, A.F., van der Maas, C.W.M., Berdowski, J.J.M., 1994. Emission database for global atmospheric research (Edgar). Environ. Monit. Assess. 31, 93–106.

Powers, J.G., Klemp, J.B., Skamarock, W.C., Davis, C.A., Dudhia, J., Gill, D.O., Coen, J.L., Gochis, D.J., Ahmadov, R., Peckham, S.E., Grell, G.A., Michalakes, J., Trahan, S., Benjamin, S.G., Alexander, C.R., Dimego, G.J., Wang, W., Schwartz, C.S., Romine, G.S., Liu, Z., Snyder, C., Chen, F., Barlage, M.J., Yu, W., Duda, M.G., 2017. The weather research and forecasting model: overview, system efforts, and future directions. Bull. Am. Meteorol. Soc. 98, 1717–1737.

Qian, J., Liao, H., Yang, Y., Li, K., Chen, L., Zhu, J., 2022. Meteorological influences on daily variation and trend of summertime surface ozone over years of 2015–2020: quantification for cities in the Yangtze River Delta. Sci. Total Environ. 834.
Rasmussen, D.J., Hu, J., Mahmud, A., Kleeman, M.J., 2013. The ozone–climate penalty: past, present, and future. Environ. Sci. Technol. 47, 14258–14266.
Ren, J., Guo, F.F., Xie, S.D., 2022. Diagnosing ozone-NOx-VOC sensitivity and revealing causes of ozoneincreases in China based on 2013–2021 satellite retrievals. Atmos. Chem. Phys. 22, 15035–15047.
Rizos, K., Meleti, C., Kouvarakis, G., Mihalopoulos, N., Melas, D., 2022. Determination of the background pollution in the Eastern Mediterranean applying a statistical clustering technique. Atmos. Environ. 276.
Roy, C., Fadnavis, S., Muller, R., Ayantika, D.C., Ploeger, F., Rap, A., 2017. Influence of enhanced Asian NOx emissions on ozone in the upper troposphere and lower stratosphere in chemistry-climate model simulations. Atmos. Chem. Phys. 17, 1297–1311.
Ruan, H.H., Zou, X.M., Scatena, E., Zimmerman, J.K., 2004. Asynchronous fluctuation of soil microbial biomass and plant litterfall in a tropical wet forest. Plant Soil 260, 147–154.
Rudeva, I., Boschat, G., Lucas, C., Ashcroft, L., Pepler, A., Hope, P., 2023. Atmospheric trends explained by changes in frequency of short-term circulation patterns. Commun. Earth Environ. 4, 127.
Saikawa, E., Kim, H., Zhong, M., Avramov, A., Zhao, Y., Janssens-Maenhout, G., Kurokawa, J., Klimont, Z., Wagner, F., Naik, V., Horowitz, L.W., Zhang, Q., 2017. Comparison of emissions inventories of anthropogenic air pollutants and greenhouse gases in China. Atmos. Chem. Phys. 17, 6393–6421.
Shang, N., Gui, K., Zhao, H., Yao, W., Zhao, H., Zhang, X., Zhang, X., Li, L., Zheng, Y., Wang, Z., Wang, Y., Che, H., Zhang, X., 2023. Decomposition of meteorological and anthropogenic contributions to near-surface ozone trends in Northeast China (2013−2021). Atmos. Pollut. Res. 14, 101841.
Shi, L., Zhu, A., Huang, L., Yaluk, E., Gu, Y., Wang, Y., Wang, S., Chan, A., Li, L., 2021. Impact of the planetary boundary layer on air quality simulations over the Yangtze River Delta region, China. Atmos. Environ. 263, 118685.
Silver, B., Reddington, C.L., Arnold, S.R., Spracklen, D.V., 2018. Substantial changes in air pollution across China during 2015–2017. Environ. Res. Lett. 13.
Simon, H., Baker, K.R., Phillips, S., 2012. Compilation and interpretation of photochemical model performance statistics published between 2006 and 2012. Atmos. Environ. 61, 124–139.
Skipper, T.N., Hu, Y., Odman, M.T., Henderson, B.H., Hogrefe, C., Mathur, R., Russell, A. G., 2021. Estimating US background ozone using data fusion. Environ. Sci. Technol. 55, 4504–4512.
Suciu, L.G., Griffin, R.J., Masiello, C.A., 2017. Regional background O3 and NOx in the Houston–Galveston–Brazoria (TX) region: a decadal-scale perspective. Atmos. Chem. Phys. 17, 6565–6581.
Tao, W.K., Wu, D., Lang, S., Chern, J.D., Peters-Lidard, C., Fridlind, A., Matsui, T., 2016. High-resolution NU-WRF simulations of a deep convective-precipitation system during MC3E: further improvements and comparisons between Goddard microphysics schemes and observations. J. Geophys. Res.-Atmos. 121, 1278–1305.
Vingarzan, R., 2004. A review of surface ozone background levels and trends. Atmos. Environ. 38, 3431–3442.
Wang, F.T., Zhang, K., Xue, J., Huang, L., Wang, Y.J., Chen, H., Wang, S.Y., Fu, J.S., Li, L., 2022a. Understanding regional background ozone by multiple methods: a case study in the Shandong Region, China, 2018–2020. J. Geophys. Res.-Atmos. 127.
Wang, J., Feng, L., Palmer, P.I., Liu, Y., Fang, S., Bösch, H., O'Dell, C.W., Tang, X., Yang, D., Liu, L., Xia, C., 2022b. Reply to: on the role of atmospheric model transport uncertainty in estimating the Chinese land carbon sink. Nature 603, E15–E16.
Wang, Y., Zhang, Y., Hao, J., Luo, M., 2011. Seasonal and spatial variability of surface ozone over China: contributions from background and domestic pollution. Atmos. Chem. Phys. 11, 3511–3525.
Wiedinmyer, C., Akagi, S.K., Yokelson, R.J., Emmons, L.K., Al-Saadi, J.A., Orlando, J.J., Soja, A.J., 2011. The Fire INventory from NCAR (FINN): a high resolution global model to estimate the emissions from open burning. Geosci. Model Dev. 4, 625–641.
World Health Organization. Regional Office for, E, 2021. Review of Evidence on Health Aspects of Air Pollution: REVIHAAP Project: Technical Report. World Health Organization. Regional Office for Europe, Copenhagen.
Wu, N., Geng, G.N., Yan, L., Bi, J.Z., Li, Y.S., Tong, D., Zheng, B., Zhang, Q., 2021. Improved spatial representation of a highly resolved emission inventory in China: evidence from TROPOMI measurements. Environ. Res. Lett. 16.
Xie, B., Fung, J.C.H., 2014. A comparison of momentum mixing models for the planetary boundary layer. J. Geophys. Res.-Atmos. 119, 2079–2091.
Xie, X., Hu, J., Qin, M., Guo, S., Hu, M., Wang, H., Lou, S., Li, J., Sun, J., Li, X., Sheng, L., Zhu, J., Chen, G., Yin, J., Fu, W., Huang, C., Zhang, Y., 2022. Modeling particulate nitrate in China: current findings and future directions. Environ. Int. 166, 107369.
Xing, J., Mathur, R., Pleim, J., Hogrefe, C., Wang, J., Gan, C.M., Sarwar, G., Wong, D.C., McKeen, S., 2016. Representing the effects of stratosphere–troposphere exchange on 3-D O3 distributions in chemistry transport models using a potential vorticity-based parameterization. Atmos. Chem. Phys. 16, 10865–10877.
Xing, J., Wang, J., Mathur, R., Wang, S., Sarwar, G., Pleim, J., Hogrefe, C., Zhang, Y., Jiang, J., Wong, D.C., Hao, J., 2017. Impacts of aerosol direct effects on tropospheric ozone through changes in atmospheric dynamics and photolysis rates. Atmos. Chem. Phys. 17, 9869–9883.
Xiong, K.L., Xie, X.D., Mao, J.J., Wang, K., Huang, L., Li, J.Y., Hu, J.L., 2023. Improving the accuracy of O3 prediction from a chemical transport model with a random forest model in the River Delta China. Environ. Pollut. 319.
Xu, M., Jin, J.B., Wang, G.Q., Segers, A., Deng, T., Lin, H.X., 2021. Machine learning based bias correction for numerical chemical transport models. Atmos. Environ. 248.
Xu, W.Y., Lin, W.L., Xu, X.B., Tang, J., Huang, J.Q., Wu, H., Zhang, X.C., 2016. Long-term trends of surface ozone and its influencing factors at the Mt Waliguan GAW station, China - part 1: overall trends and characteristics. Atmos. Chem. Phys. 16, 6191–6205.
Xue, C., Ye, C., Zhang, C., Catoire, V., Liu, P., Gu, R., Zhang, J., Ma, Z., Zhao, X., Zhang, W., Ren, Y., Krysztofiak, G., Tong, S., Xue, L., An, J., Ge, M., Mellouki, A., Mu, Y., 2021. Evidence for strong HONO emission from fertilized agricultural fields and its remarkable impact on regional O3 pollution in the summer North China Plain. ACS Earth Space Chem. 5, 340–347.
Xue, J., Wang, F., Zhang, K., Zhai, H., Jin, D., Duan, Y., Yaluk, E., Wang, Y., Huang, L., Li, Y., Lei, T., Fu, Q., Fu, J.S., Li, L., 2023. Elucidate long-term changes of ozone in Shanghai based on an integrated machine learning method. Front. Environ. Sci. Eng. 17, 138.
Yan, X., Xu, E.H., Ieee., 2020. ARIMA and multiple regression additive models for PM2.5 based on linear interpolation. In: International Conference on Big Data and Artificial Intelligence and Software Engineering (ICBASE). Chengdu, PEOPLES R CHINA.
Ye, X.P., Wang, X.L., Zhang, L., 2022. Diagnosing the model bias in simulating daily surface ozone variability using a machine learning method: the effects of dry deposition and cloud optical depth. Environ. Sci. Technol. 56, 16665–16675.
Yi, X., Sarwar, G., Bian, J.T., Huang, L., Li, Q.Y., Jiang, S., Liu, H.Q., Wang, Y.J., Chen, H., Wang, T., Chen, J.M., Saiz-Lopez, A., Wong, D.C., Li, L., 2023. Significant impact of reactive chlorine on complex air pollution over the Yangtze River Delta Region, China. J. Geophys. Res.-Atmos. 128.
Yue, X., Unger, N., Harper, K., Xia, X.G., Liao, H., Zhu, T., Xiao, J.F., Feng, Z.Z., Li, J., 2017. Ozone and haze pollution weakens net primary productivity in China. Atmos. Chem. Phys. 17, 6073–6089.
Zhang, G., Xue, H., Xu, J., Chen, J., He, H., 2016a. The WRF performance comparison based on Noah and Noah-MP land surface processes on East Asia. Meteorol. Monthly 42, 1058–1068.
Zhang, J., Wang, P., Li, J.Y., Mendola, P., Sherman, S., Ying, Q., 2016b. Estimating population exposure to ambient polycyclic aromatic hydrocarbon in the United States - part II: source apportionment and cancer risk assessment. Environ. Int. 97, 163–170.
Zhang, Y., Wang, W., Wu, S.-Y., Wang, K., Minoura, H., Wang, Z., 2014. Impacts of updated emission inventories on source apportionment of fine particle and ozone over the southeastern U.S. Atmos. Environ. 88, 133–154.
Zheng, B., Tong, D., Li, M., Liu, F., Hong, C., Geng, G., Li, H., Li, X., Peng, L., Qi, J., Yan, L., Zhang, Y., Zhao, H., Zheng, Y., He, K., Zhang, Q., 2018. Trends in China's anthropogenic emissions since 2010 as the consequence of clean air actions. Atmos. Chem. Phys. 18, 14095–14111.
Zheng, Y.X., Xue, T., Zhang, Q., Geng, G.N., Tong, D., Li, X., He, K.B., 2017. Air quality improvements and health benefits from China's clean air action since 2013. Environ. Res. Lett. 12.
Zheng, Z., Li, K., Xu, B., Dou, J., Li, L., Zhang, G., Li, S., Geng, C., Yang, W., Azzi, M., Bai, Z., 2023. O3–precursor relationship over multiple patterns of timescale: a case study in Zibo, Shandong Province, China. Atmos. Chem. Phys. 23, 2649–2665.
Zhou, L.T., Huang, R., 2014. Regional differences in surface sensible and latent heat fluxes in China. Theor. Appl. Climatol. 116, 625–637.